ACS APPLIED ENERGY MATERIALS

www.acsaem.org

Article

Effect of Oxidation on the Mechanochemical Synthesis of Bismuth Telluride Nanophases, Ex Situ and In Situ Structural Characterization, and Thermoelectric Properties

Marcelo Augusto Malagutti, Rayner Enriquez Camps, Umberto Anselmi-Tamburini, Robert E. Dinnebier, Claudia Weidenthaler, Paolo Scardi, and Carlos Eduardo Maduro de Campos*

Cite This: *ACS Appl. Energy Mater.* 2026, 9, 6608−6621

Read Online

ACCESS | Metrics & More | Article Recommendations | Supporting Information

ABSTRACT: The Bi–Te system remains one of the most extensively studied thermoelectric materials and is among the few commercially viable solutions for waste heat recovery. However, the role of synthesis conditions—particularly precursor oxidation—on phase formation and transport properties remains insufficiently understood. In this work, we investigate the effect of chemical composition and precursor oxidation on the polymorphism and thermoelectric performance of mechanochemically synthesized, low-density Bi_xTe_{100-x} (x = 50 and 70) nanomaterials. High-energy ball milling enables rapid phase formation within minutes, yielding distinct phase compositions depending on precursor form and oxidized contaminations. For $Bi_{50}Te_{50}$, highly oxidized precursors stabilize Bi_2Te_3, moderately oxidized conditions favor BiTe, and low-oxide precursors promote the formation of Bi_4Te_3, while Bi_2Te is obtained for $Bi_{70}Te_{30}$. In situ X-ray diffraction reveals rapid phase formation on short timescales, strongly dependent on precursor oxidation. Highly oxidized precursors also induce ternary oxide phases that significantly suppress electrical transport. Despite this, a compensating reduction in thermal conductivity leads to a maximum zT of 0.18 at 200 °C for the Bi_2Te_3 phase. Analysis of the thermoelectric quality factor demonstrates that oxidation ultimately degrades intrinsic electronic performance, indicating that zT alone can be misleading when comparing materials with different microstructures and porosity. Additional densification via spark plasma sintering improves room-temperature performance but highlights the competing increase in electronic thermal conductivity, further supporting the need to evaluate intrinsic material quality beyond zT. These results establish mechanochemistry as a versatile route for accessing a wide range of Bi–Te polymorphs and highlight the critical role of precursor oxidation in achieving optimal thermoelectric performance.

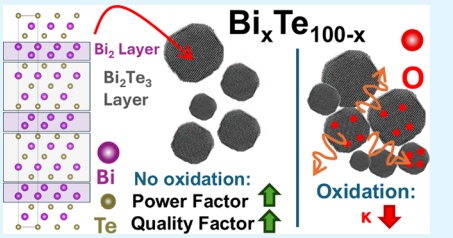

KEYWORDS: *thermoelectricity, chalcogenides, nanomaterials, mechanochemistry, rietveld-XRD*

1. INTRODUCTION

Thermoelectric (TE) materials enable direct conversion between thermal and electrical energy via the Seebeck and Peltier effects. The growing interest in TE materials stems from their high reliability and the absence of moving parts, which make them particularly suitable for remote and off-grid applications such as aerospace systems, including the Voyager and Cassini missions,[1] as well as for powering Internet of Things (IoT) devices.[2] In addition, TE materials are widely used in microcooling and microheating technologies, light-generation systems, and waste heat recovery from sources such as solar cells, motors, and industrial processes.[3−10]

The efficiency of converting heat to electrical energy in TE materials is characterized by the dimensionless figure of merit, zT.[11] It is defined as $zT = \frac{S^2\sigma}{\kappa}T$, where S is the Seebeck coefficient, σ is the electrical conductivity, T is the absolute temperature, and $\kappa = \kappa_L + \kappa_{el}$ is the total thermal conductivity, consisting of lattice (κ_L) and electronic (κ_{el}) contributions.[11−13] These transport parameters are strongly interdependent, making the optimization of the zT inherently challenging.[3,14,15] For example, increasing the carrier concentration—through intrinsic or extrinsic doping—generally enhances electrical conductivity but tends to reduce the Seebeck coefficient, potentially lowering the overall figure of merit. Strategies to partially decouple these relationships have been successfully implemented in materials containing heavy elements and layered crystal structures, such as bismuth tellurides (Bi–Te).[16−18] These compounds exhibit a high band degeneracy in the electronic density of states, providing multiple transport channels without significantly increasing carrier concentration, which is beneficial for maintaining a high Seebeck coefficient. Moreover, the strongly anisotropic electronic band structure of Bi_2Te_3 enables a large density-of-states effective

Received: March 18, 2026
Revised: April 13, 2026
Accepted: April 16, 2026
Published: April 29, 2026

https://doi.org/10.1021/acsaem.6c00972
ACS Appl. Energy Mater. 2026, 9, 6608−6621

mass while preserving a low transport effective mass and high carrier mobility.[3,14,15] For these reasons, since their first TE applications in the 1950s,[13] Bi–Te-based materials have remained the benchmark for near room-temperature TE performance and continue to dominate technologies for power generation, cooling, and temperature control in optoelectronic devices.[16−18]

High-energy ball-milling is a mechanochemical synthesis technique that aligns well with several principles of green chemistry, offering a potentially sustainable route for materials processing.[19] It enables large-scale production while reducing fabrication costs and can promote the formation of metastable and highly disordered nanostructures.[20−23] In a top-down approach, ball milling is used to induce nanostructuring effects in Bi–Te materials synthesized through solid-state reactions, inducing the phonon-glass electron-crystal (PGEC) behavior.[24−29] This strategy consists of reducing the crystallite size (CS) of polycrystalline TE materials to the nanoscale, generating a high density of interfaces that act as energy filters. In this case, these interfaces preferentially scatter low-energy charge carriers that mainly contribute to heat transport, while allowing higher-energy carriers, which contribute more effectively to the Seebeck effect, to pass with less resistance.[17,30,31] Alternatively, Bi–Te materials can also be synthesized through a bottom-up approach involving ball-milling of precursors followed by consolidation via spark plasma sintering (SPS).[26,32] While these methods enable rapid phase formation and nanostructuring, they also introduce defects, disorder, and porosity, which can strongly influence TE transport properties. Despite extensive studies on the mechanochemical synthesis of Bi–Te materials, the role of precursor oxidation in governing phase formation and TE performance remains poorly understood.

In this work, we systematically investigate the influence of precursor oxidation and milling conditions on phase selection and TE performance in Bi_xTe_{100-x} systems. For the $Bi_{50}Te_{50}$ composition, three distinct phases (Bi_2Te_3, BiTe, and Bi_4Te_3) are selectively stabilized depending on oxidation level and milling conditions, all exhibiting n-type semiconducting behavior. In contrast, $Bi_{70}Te_{30}$ compositions display p-type behavior with comparatively limited sensitivity to precursor oxidation, resulting in consistent structural characteristics. TE performance was evaluated through measurements of Seebeck coefficient, electrical conductivity, and thermal conductivity, complemented by densification via SPS. Although highly oxidized samples exhibit higher zT due to reduced thermal conductivity, analysis of the TE quality factor reveals a degradation of intrinsic electronic performance. This indicates that the apparent improvement in zT arises from extrinsic effects and suggests that lower-oxidation materials may achieve superior performance upon full optimization. Furthermore, SPS improves room-temperature transport properties but highlights the competing increase in electronic thermal conductivity. Overall, these results demonstrate that precursor oxidation plays a critical role in governing phase formation and transport properties and emphasize the importance of distinguishing intrinsic material quality from extrinsic contributions when optimizing TE performance.

2. EXPERIMENTAL DETAILS

2.1. Sample Preparation

Elemental powders and granules of Bi and Te were mixed under an argon atmosphere in two different proportions, viewing the chemical compositions of $Bi_{50}Te_{50}$ and $Bi_{70}Te_{30}$. The samples with $Bi_{50}Te_{50}$ composition were prepared using two different Te sources (Sigma-Aldrich 264865-25G powder, −30 mesh, ≥99.997% trace metal basis and Sigma-Aldrich 263303-25G granular, −5 to +50 mesh, ≥99.99% trace metal basis). Careful analysis of the starting materials revealed non-negligible levels of oxidation for Te (see values in Table 1), higher for the powder source, as well as for the Bi powder (Sigma-Aldrich 265462-100G powder, −100 mesh, 99% trace metal basis). XRD data and Rietveld profile fitting (performed using TOPAS[33]) are provided in Supplementary Note 1, in Figure S1. The stainless-steel vials of 65 mL volume and sets of 9 stainless steel balls were used, being 3 balls of 12.7 mm (½ inch) in diameter and 6 of 6.35 mm (¼ inch) diameter. The initial ball-to-powder ratio (BPR) was 10 for all samples. The mechanical energy was provided by a dual vial shaker mill SPEX 8000D that shakes the vials in a complex motion combining 5.9 cm back-and-forth swings with short (2.5 cm) lateral movements, each end of the vial describing a figure-8 at a speed of 875 cycles/minute. After every 3 h of milling, a small number of samples were collected for ex situ analysis. All procedures were carried out in a glove bag filled with argon.

Five samples (two $Bi_{50}Te_{50}$ and three $Bi_{70}Te_{30}$) were produced using a modified (MM400 Retsch) ball mill,[34] shaking horizontally with a frequency of 20 Hz, and special 25 mL stainless steel jars with windows (covered with PMMA and metal rings). Two stainless steel balls of 15 mm were used, and a BPR of 20 was chosen to result in about 1.4 g of sample in each batch. Two batches of $Bi_{50}Te_{50}$ composition and three of $Bi_{70}Te_{30}$ were produced. For that, high-purity Te (Sigma-Aldrich 266418-100G powder, −200 mesh, ≥99.8% trace metal basis) and Bi (Sigma-Aldrich 95372-100G granular, ≥99.99% trace metal basis) sources were used. No oxidation was detected for the Te powder and Bi granules used in real-time mechanochemical synthesis experiments (Figure S1 and Table 1). All sample preparations were performed in a glove box filled with argon.

The sample labeling for the powders used and the ball-milling setup employed are given in Tables 1 and 2, respectively. Granular materials are identified with the letter G, while micrometer-sized powders are labeled by the letter P. The use of the SPEX-8000D mill is referred to as BM1, while the Retsch MM400 mill is denoted as BM2.

2.2. X-ray Diffraction Experiments

The XRD measurements were performed in six different diffractometers, including the laboratory sources/setups Xpert MPD, Stoe, Empyrean, D8 and, the XRPD beamlines at ESRF,[35,36] MAX-IV,[35] and DESY[37−39] synchrotron sources. The list of all the experiments and their descriptions are available in Supplementary Note 2, Table S1. For Rietveld analysis and profile fitting, the program package TOPAS 7 academic version[33] was used.

2.3. Raman Analysis

Raman spectra were acquired using a Renishaw inVia confocal Raman microscope coupled to a Leica DM2700M optical microscope. The system was equipped with a Renishaw RL785 laser (maximum output power 256 mW) and a Renishaw Centrus 5MX233 detector, controlled via WiRe 5.6 software. Measurements were performed in backscattering geometry using a 785 nm excitation wavelength with a 1200 lines/mm diffraction grating and a 20× objective. Data were collected in regular static-scan mode with 10 s acquisition time at 1% laser power. All spectra were obtained under ambient conditions, ensuring stable focus and minimizing sample heating during measurement.

2.4. Thermal Analysis

The differential thermal analysis (DTA) made use of a NETZSCH STA 449F5 instrument, employing an Ar flow of 50 mL min^{-1}. The samples were loaded in 0.3 mL Al_2O_3 crucibles. A 5 °C min^{-1} ramp was applied for the heating, from 22 to 600 °C. Cooling ramps were measured within the same temperature range and ramp.

In situ high-temperature X-ray powder diffraction (HTXRPD) was performed using a Stadi P diffractometer (Stoe) in Debye–Scherrer

https://doi.org/10.1021/acsaem.6c00972
ACS Appl. Energy Mater. 2026, 9, 6608−6621

Table 1. Reactants Used in Mechanochemical Synthesis

	ID	reactant	form	supplier (product code)	particle size	nominal purity	% oxide by XRD
I	Bi_P	Bi	powder	Sigma-Aldrich (265462)	100 mesh	99%	22(1) % of Bi_2O_3
II	Bi_G	Bi	granular	Sigma-Aldrich (95372)		≥99.99%	
III	Te_P1	Te	powder	Sigma-Aldrich (264865)	−30 mesh	≥99.997%	57–83 % of TeO_2
IV	Te_G	Te	granular	Sigma-Aldrich (263303)		≥99.99%	<3 % of TeO_2
V	Te_P2	Te	powder	Sigma-Aldrich (266418)	200 mesh	≥99.8%	<1 % of TeO_2

Table 2. Sample Names and Milling Conditions

sample	composition	Bi source	Te source	mill	vessel	BPR	balls	final milling time
1-Bi50Te-BM1a	$Bi_{50}Te_{50}$	Bi_P	Te_P1	SPEX 8000D	65 mL	10	3 × 12.7 mm 6 × 6.35 mm	9 h
2-Bi50Te-BM1b	$Bi_{50}Te_{50}$	Bi_P	Te_G	SPEX 8000D	65 mL	10	3 × 12.7 mm 6 × 6.35 mm	15 h
3-Bi50Te-BM2a	$Bi_{50}Te_{50}$	Bi_G	Te_P2	Retsch MM400	25 mL	20	2 × 15 mm	24.8 min
4-Bi50Te-BM2b	$Bi_{50}Te_{50}$	Bi_G	Te_P2	Retsch MM400	25 mL	20	2 × 15 mm	24.8 min
5-Bi70Te-BM1	$Bi_{70}Te_{30}$	Bi_P	Te_G	SPEX 8000D	65 mL	10	3 × 12.7 mm 6 × 6.35 mm	15 h
6-Bi70Te-BM2a	$Bi_{70}Te_{30}$	Bi_G	Te_P2	Retsch MM400	25 mL	20	2 × 15 mm	25.0 min
7-Bi70Te-BM2b	$Bi_{70}Te_{30}$	Bi_G	Te_P2	Retsch MM400	25 mL	20	2 × 15 mm	28.3 min
8-Bi70Te-BM2c	$Bi_{70}Te_{30}$	Bi_G	Te_P2	Retsch MM400	25 mL	20	2 × 15 mm	45.2 min

geometry. Ag $K\alpha_1$ radiation, which came from a Ge(111)-Johann-type monochromator, was used, and a triple Mythen 1K detector array (Dectris) was employed for data collection. Samples were sealed both in Ar and air-filled environment, using 0.3 mm quartz-glass capillaries (Hilgenberg glass) and spun during measurement. Heating was performed using a GSB 1300 gas blower (FMB Oxford) at 5 K/min. HTXRD was conducted from 30 to 650 °C, with 1 h measurement time.

2.5. Morphological, Chemical, and Electron Diffraction Characterization

The ZEISS DSM 982 Gemini was used for scanning electron microscopy (SEM) imaging. It is equipped with SE, BSE, and EDX detectors. The EM ACE 600 coater was used for Ir coating of the samples disposed of over metal stubs.

For transmission electron microscopy (TEM) analysis, the powders were dispersed in ethanol, sonicated in an ultrasonic bath, and then deposited onto carbon-coated copper grids (FCF 300Cu). Particle size measurements from TEM images were performed using the open-source software FIJI (ImageJ).[40] For micrographs showing rounded or quasi-spherical particles, the Oval Selection tool was employed to measure the maximum diameter of each particle. In cases of irregular or elongated morphologies, the Straight-Line tool was used to determine the largest dimension. All images were rescaled to nanometers using the corresponding scale bars, and all discernible particles were included in the histograms except those located at image edges or overlapping, which were excluded to minimize measurement uncertainties.

The BM1-processed samples were analyzed using a JEOL ARM200F image-corrected transmission electron microscope. TEM, high-resolution TEM (HR-TEM), and selected area electron diffraction (SAED) images were acquired. In contrast, the BM2-prepared samples were characterized using a JEOL JEM-1400, operating at 120 kV, from which TEM images and SAED patterns were obtained. The SAED patterns were indexed using the CrysTBox software[41] from the structural data obtained from Rietveld-XRD analysis.

2.6. TE Characterization

The Bi-Te as-milled powders were cold-pressed into 16 mm-diameter cylindrical pellets with a thickness of approximately 1.0 mm by applying a load of ∼15 tons for 5 min under an Ar atmosphere. They were thermally treated in a static atmosphere of Ar for 120 min at 300° C (ramp 3° C min^{-1}) and naturally cooled down to room temperature. The as-milled 6-Bi70Te-BM2a powder was further sintered by SPS at 400 °C for 10–15 min under 50 MPa using a WC die. A boron nitride layer was applied to prevent current flow through the sample and contamination from the die.

The absolute Seebeck coefficient and resistivity were measured in a four-contact configuration and with a Pt standard using a Linseis Messgeraete GmbH's LSR-3 instrument. Measurements were performed under a static He atmosphere (pressure ∼ 0.2 bar) in the range from room temperature (RT) to 250 °C, with a heating rate of 10 K min^{-1} and a temperature gradient across the sample of ∼10 K. Temperature-dependent thermal diffusivity measurements followed the same temperature limits and were performed using a laser flash Linseis Messgeraete GmbH's LFA 500 under vacuum. A declared instrumental accuracy of 3% should be considered for thermal diffusivity. Thermal conductivity is calculated as $\kappa = \alpha\rho C_p$, where α is thermal diffusivity, ρ is the density, and C_p is the specific heat. C_p was estimated using the Neumann−Kopp law, and density was estimated using the geometric method. Values are reported in Table S2 of the Supplementary Note 2.

Electrical resistivity, carrier concentration, and mobility were determined using Hall-effect measurements performed in a Van der Pauw configuration with a Linseis HCS-1 system. All measurements were conducted under a nitrogen atmosphere over the temperature range of 30−200 °C.

3. RESULTS AND DISCUSSION

3.1. X-ray Powder Diffraction Analysis

The XRD analysis of the $Bi_{50}Te_{50}$ and $Bi_{70}Te_{30}$ systems (Figure 1) reveals that phase formation is strongly governed by precursor chemistry and milling conditions, leading to distinct structural outcomes and oxidation behavior.

For the $Bi_{50}Te_{50}$ samples, three distinct phases were identified: Bi_2Te_3 Tellurobismuthite (PDF #04-004-8858) for sample 1-Bi50Te-BM1a, BiTe Tsumoite (PDF #04-008-8271) for

https://doi.org/10.1021/acsaem.6c00972
ACS Appl. Energy Mater. 2026, 9, 6608−6621

sample 2-Bi50Te-BM1b, and Bi_4Te_3 Pilsinite (PDF #00-033-0216) for sample 3-Bi50Te-BM2. The corresponding diffraction patterns and Rietveld refinements are shown in Figure 1, with detailed fitting parameters reported in Supplementary Note 2 (Figures S2–S7 and Table S3). Complementary Raman spectroscopy (Supplementary Note 2.1) further confirms the phase identification through comparison with reference spectra.[42−49]

A key feature of the $Bi_{50}Te_{50}$ samples is the presence of secondary Bi–Te–O phases (Figure 1, black asterisks), which originate from oxidation of Te-containing precursors. This effect is particularly evident in samples 1 and 2, whereas it is effectively suppressed in sample 3, where the reagents were never exposed during synthesis. These results highlight the critical role of precursor handling in controlling phase purity.

In contrast, the $Bi_{70}Te_{30}$ system exhibits a markedly different behavior. XRD patterns indicate the formation of a single dominant Bi_2Te phase across all milling conditions and reagent types, demonstrating a reduced sensitivity to oxidation. Minor Fe contamination is observed in sample 5-Bi70Te-BM1 (red asterisks in Figure 1), likely originating from the milling media. Variations in peak intensities are observed between samples, which can be attributed to microstructural effects such as stacking faults or Te–Bi interstitial defects. However, a quantitative description of these features from room-temperature XRD alone remains challenging and will be further addressed in the following sections.

The evolution of structural and microstructural parameters with milling time indicates that phase formation occurs rapidly under all investigated conditions. As shown in Figures S9–S11, Bi–Te phases are stabilized within the first hours of milling. For example, in sample 1-Bi50Te-BM1a, lattice parameters stabilize after ∼3 h, while crystallite size (CS) and microstrain (MS) show only minor changes up to 9 h. Similarly, sample 2-Bi50Te-BM1b achieves phase purity above 96% with stable structural parameters over time (Figure S10). A significantly faster reaction is observed for BM setup #2, where the higher ball-to-powder ratio enables stabilization of the Bi_4Te_3 phase within 25 min (sample 3-Bi50Te-BM2a), in agreement with rapid formation reported in chemically synthesized systems.[50] For the $Bi_{70}Te_{30}$ sample, phase stabilization occurs within the first hour of milling, although prolonged processing leads to increased Fe contamination (Figure S11). For the $Bi_{70}Te_{30}$ sample, phase stabilization occurs within the first hour of milling, although prolonged processing leads to increased Fe contamination (Figure S11).

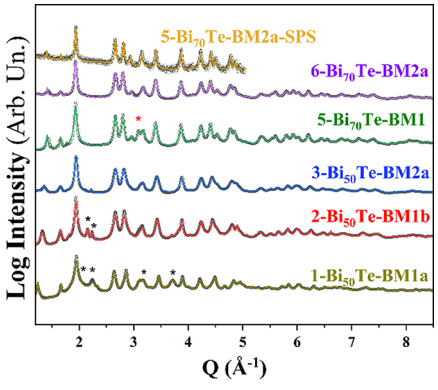

Figure 1. XRD data (black dots) of all the Bi−Te compounds and the corresponding Rietveld profile fitting (colored lines). The black * corresponds to the Bi−Te−O ternary phases, and the red * to the Fe contamination from the milling media.

Overall, these results demonstrate that mechanochemical synthesis enables rapid stabilization of Bi–Te phases, while the final phase composition and microstructure are primarily dictated by precursor chemistry, oxidation effects, and milling parameters. In particular, Bi-rich compositions ($Bi_{70}Te_{30}$) are less prone to oxidation than $Bi_{50}Te_{50}$, due to the lower oxide content in Bi precursors compared to Te-based reagents.

3.2. In Situ XRD with Temperature and DTA-TG Experiments

Thermal stability is a critical parameter for TE materials, as it defines their operational temperature range. To evaluate this aspect, differential/thermogravimetric analysis (DTA/TGA) and in situ high-temperature X-ray diffraction (HTXRPD) measurements were performed up to 650 °C on oxide-containing samples (1-Bi50Te-BM1a, 1-Bi50Te-BM1b, 5-Bi70Te-BM1; see Table S1). The influence of air exposure was examined by performing HTXRPD experiments in both air-filled and argon-filled capillaries.

Overall, the results reveal a clear hierarchy in thermal stability among the phases investigated. The Bi_2Te_3 tellurobismuthite phase exhibits the highest stability, remaining largely stable up to 650 °C under argon, as shown by the HTXRPD patterns in Figure 2a. The corresponding phase evolution (Figure 2b) indicates that, although Bi_2Te_3 remains dominant, secondary Bi–Te–O phases begin to form above ∼400 °C, as evidenced by the appearance of additional reflections attributed to Bi_2TeO_5 and Bi_2TeO_2. These transformations are further supported by DTA measurements (Figure 3a), where exothermic events observed during cooling at ∼545–564 °C are associated with the formation and crystallization of these oxide phases.

In contrast, the BiTe (tsumoite) phase shows lower thermal stability. As illustrated in Figure 4a–c, BiTe remains stable up to ∼500 °C, after which it undergoes phase transformations that depend strongly on the atmosphere. In argon (Figure 4a), the phase progressively decomposes at higher temperatures, whereas in air (Figure 4b), oxidation dominates, leading to the formation of Bi_2TeO_7 above ∼500 °C. The corresponding phase fractions (Figure 4c) clearly highlight this divergence in reaction pathways. DTA analysis (Figure 3a) further reveals endothermic features near ∼548 °C, consistent with the onset of BiTe instability and partial melting. These results confirm that BiTe is intrinsically less stable than Bi_2Te_3 and more sensitive to environmental conditions.

An even lower thermal stability is observed for Bi-rich compositions, such as the 5-Bi70Te-BM1 sample. The HTXRPD data (Figure 5a) show that, under argon, the Bi_2Te phase decomposes at temperatures as low as ∼300 °C. When exposed to air (Figure 5b), the degradation follows a different pathway, leading to the formation of metallic Bi and oxide phases, as quantified in Figure 5c. This behavior is consistent with the DTA results (Figure 3b), where a weak endothermic signal near ∼400 °C corresponds to the peritectic decomposition of Bi_2Te, followed by a clear melting event of Bi at ∼263 °C during subsequent heating. Cooling cycles reveal Bi recrystallization near ∼255 °C. No significant mass loss is detected, indicating that the observed transformations are primarily structural.

The observed differences in thermal stability can be rationalized based on crystal structure. Bi_2Te_3 consists of stable quintuple layers, whereas BiTe and Bi-rich phases contain mixed

https://doi.org/10.1021/acsaem.6c00972
ACS Appl. Energy Mater. 2026, 9, 6608−6621

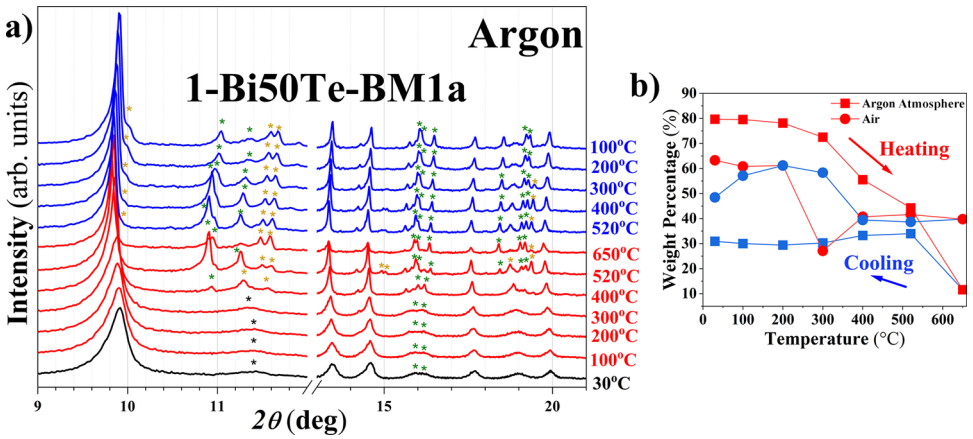

Figure 2. (a) High-temperature X-ray diffraction patterns of the 1-Bi50Te-BM1a sample. Red corresponds to the heating curves and blue to the cooling ramps. The yellow and green asterisks correspond to Bi_2TeO_5 (*I*4/*mmm*) and Bi_2TeO_2 (*Abm*2) Bragg peaks. (b) Bi_2Te_3 phase percentage with temperature for the capillary filled in Ar (squared) and air (circle) atmospheres. Red corresponds to the heating curves, whereas blue corresponds to the cooling ramps.

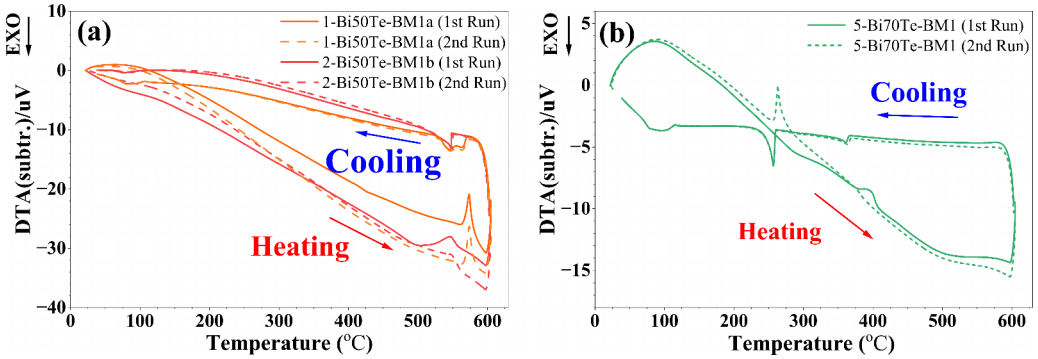

Figure 3. DTA analysis of the (a) Bi50Te and (b) Bi70Te samples.

Bi and Bi_2Te_3 sublayers, resulting in reduced structural stability and lower decomposition temperatures[24] (vide graphical representation in Figure 7a). Consequently, phases with higher Bi content not only decompose more readily but also exhibit a stronger dependence on oxygen exposure, leading to distinct oxidation pathways.

From an application perspective, these results indicate that the operating temperature of these materials should remain below ~400 °C to prevent degradation and oxidation, regardless of the atmosphere. A detailed summary of decomposition temperatures is provided in Table S6 (Supplementary Note 3).

3.3. Electron Microscopy (SEM, TEM, and HR-TEM), Diffraction and Chemical Analysis

Stacking faults and anisotropic crystallite shapes arising from the intrinsic lamellar structure of Bi–Te phases are well-documented issues.[24] To confirm their presence in the materials studied here—and to establish their connection to the TE properties discussed in the following sections—we present complementary microscopy measurements.

In Figure 6, TEM micrographs confirm that all samples exhibit nanosized crystalline domains, well dispersed over the carbon-covered Cu grids, with broad size distributions consistent with the nature of the milling process. Low-magnification images (Figure 6, first column) reveal morphological differences among the milling conditions: sample 1-Bi50Te-BM1a displays irregular crystallites, whereas 2-Bi50Te-BM1b and 5-Bi70Te-BM1 show more homogeneous, quasi-spherical domains with better-defined shapes. Particle size histograms display broad, approximately log-normal distributions, with mean values ranging from ~20 to 50 nm, depending on stoichiometry, precursor morphology, and the effect of thermal treatment. More details are found in the Supplementary Note 2.3 (Figures S12 and S13). Overall, the average sizes obtained by TEM are slightly smaller than those derived from XRPD (Rietveld refinement, Table S3). This discrepancy, commonly observed in comparative studies, can be ascribed to the difference between crystallite size (XRPD) and particle size definitions as directly observed by TEM, as well as to the statistical influence of the analyzed area (vide comments in Refs.[21,22]. Furthermore, although TEM images revealed a high representation of isolated particles (Figure 6, first column), agglomerates were also detected, which contributed to the larger values recorded by XRPD due to the inclusion of larger domains and visible aggregates (see Supplementary Note 4 for SEM and EDS analysis of the agglomerated particles).

Crystalline morphology influences the response to thermal treatment. Samples recovered from DTA, namely BM1a-tt, BM1b-tt, and BM1-tt, present different behavior depending on the phase stabilized. BM1a-tt exhibits an increase in crystallite size and a broader distribution, while the opposite trend

https://doi.org/10.1021/acsaem.6c00972
ACS Appl. Energy Mater. 2026, 9, 6608−6621

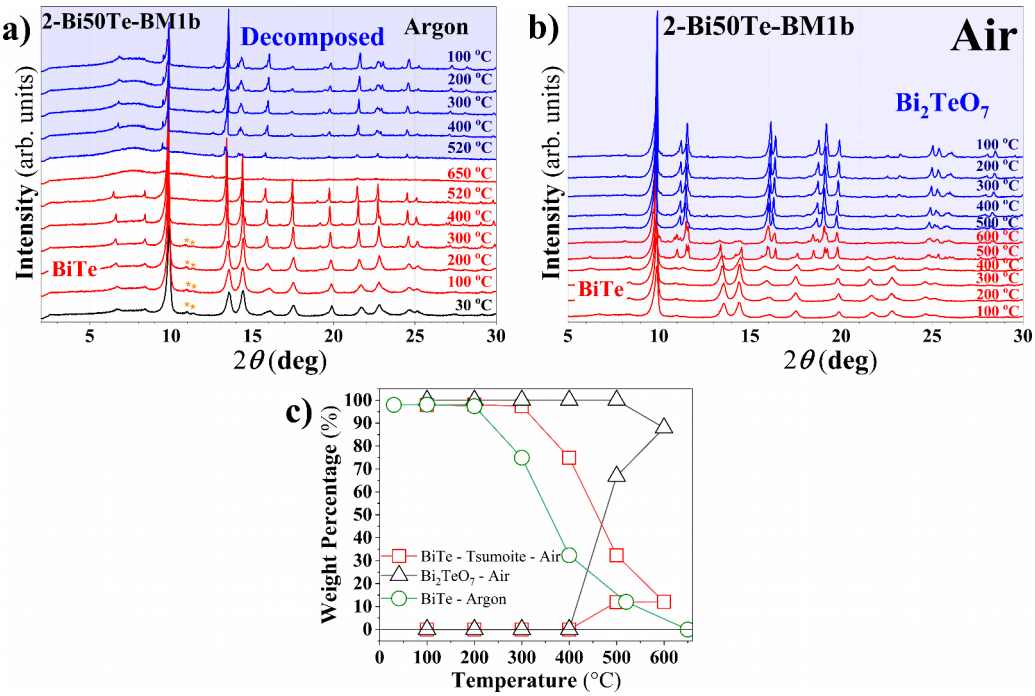

Figure 4. High-temperature X-ray diffraction patterns of the 2-Bi50Te-BM1b sample measured in (a) argon and (b) air atmospheres. (c) Phase weight fraction with temperature. The yellow asterisks correspond to the Bi_2TeO_5 (*I*4/*mmm*) Bragg peaks. The decomposed phase in item a was not identified. Error bars are smaller than symbols.

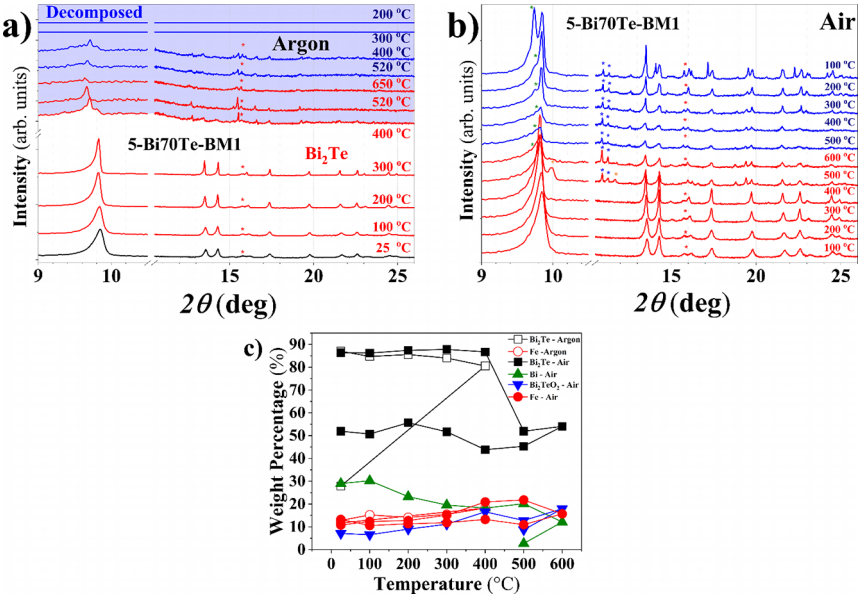

Figure 5. High-temperature X-ray diffraction patterns of the 5-Bi70Te-BM1 sample measured in (a) argon and (b) air atmospheres. (c) Change of weight fraction with temperature. The asterisks in items a and b correspond to the peaks of the phases, with color indicated in item (c). Error bars are smaller than symbols.

occurs for BM1b-tt and BM1-tt (see Figure 6). We also observe that the particle size distribution broadened for the BM1a-tt sample, whereas the others showed narrowing after heating. The BM1a-tt sample consists predominantly of the Bi_2Te_3 phase, which is thermodynamically more stable than the Bi_2Te, BiTe, and Bi_4Te_3 phases.[24,25] This higher stability arises from its crystal structure, composed solely of Bi_2Te_3 quintuple layers, whereas the other phases are built from alternating Bi_2 and Bi_2Te_3 layers,[24,25] as schematically represented in Figure 7a. Owing to its structural robustness, Bi_2Te_3 undergoes the expected coalescence behavior during thermal treatment, leading to crystallite growth and a broader size distribution. In contrast, the less stable phases (Bi_2Te, BiTe, and Bi_4Te_3) decompose upon heating, as evidenced in Figure 4a

https://doi.org/10.1021/acsaem.6c00972
ACS Appl. Energy Mater. 2026, 9, 6608−6621

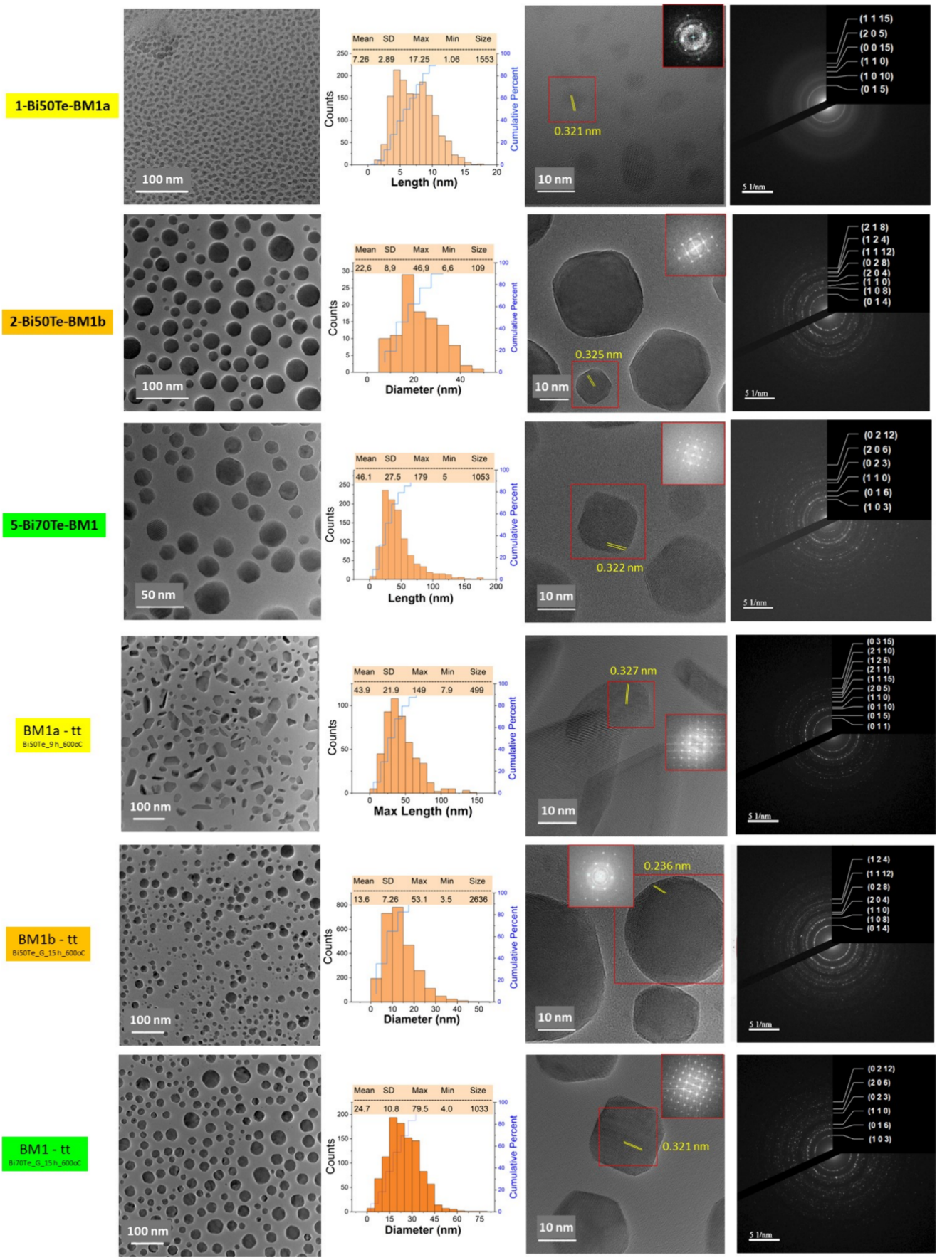

Figure 6. Transmission electron microscopy (TEM) characterization of as-milled samples and those recovered after DTA analysis (identified with 'tt' in the sample code). For each sample, the first column shows bright-field TEM images, the second column presents particle size distribution

https://doi.org/10.1021/acsaem.6c00972
ACS Appl. Energy Mater. 2026, 9, 6608−6621

Figure 6. continued

histograms, the third column displays HR-TEM images with corresponding fast Fourier transform (FFT) insets, and the fourth column shows selected area electron diffraction (SAED) patterns indexed with the corresponding Miller indices. Sample codes are indicated to the left of each row.

(for 2-Bi50Te-BM1b) and Figure 5a (for Bi70Te-BM1). Upon cooling, these samples recrystallize, but the broader diffraction peaks indicate smaller crystallite sizes.

HR-TEM images (Figure 6, third column) reveal layered particles with rounded to hexagonal morphologies, where well-defined lattice fringes are distinguished. These results confirm that, even after mechanical milling, the crystalline order is preserved at the nanoscale. Complementarily, SAED (Figure 6, fourth column) patterns show polycrystalline rings that could be satisfactorily indexed in agreement with the structural analysis obtained from XRPD-Rietveld refinements, thus corroborating the phase identification.

In addition, HR-TEM lattice spacing measurements further corroborate the structural assignments in Figure 6. For sample 1-Bi50Te-BM1a, interplanar distances of 0.321 and 0.327 nm were obtained, which can be indexed to reflections such as the (015) plane of rhombohedral Bi_2Te_3. Sample 2-Bi50Te-BM1b shows lattice spacings of 0.325 and 0.236 nm, which correspond to the (014) and (110) planes, respectively, in agreement with the reported BiTe structure. Finally, for 5-Bi70Te-BM1, measured spacings of 0.322 and 0.321 nm are compatible with reflections such as the (013) plane of the Bi_2Te phase. HR-TEM also allows a better phase identification for the

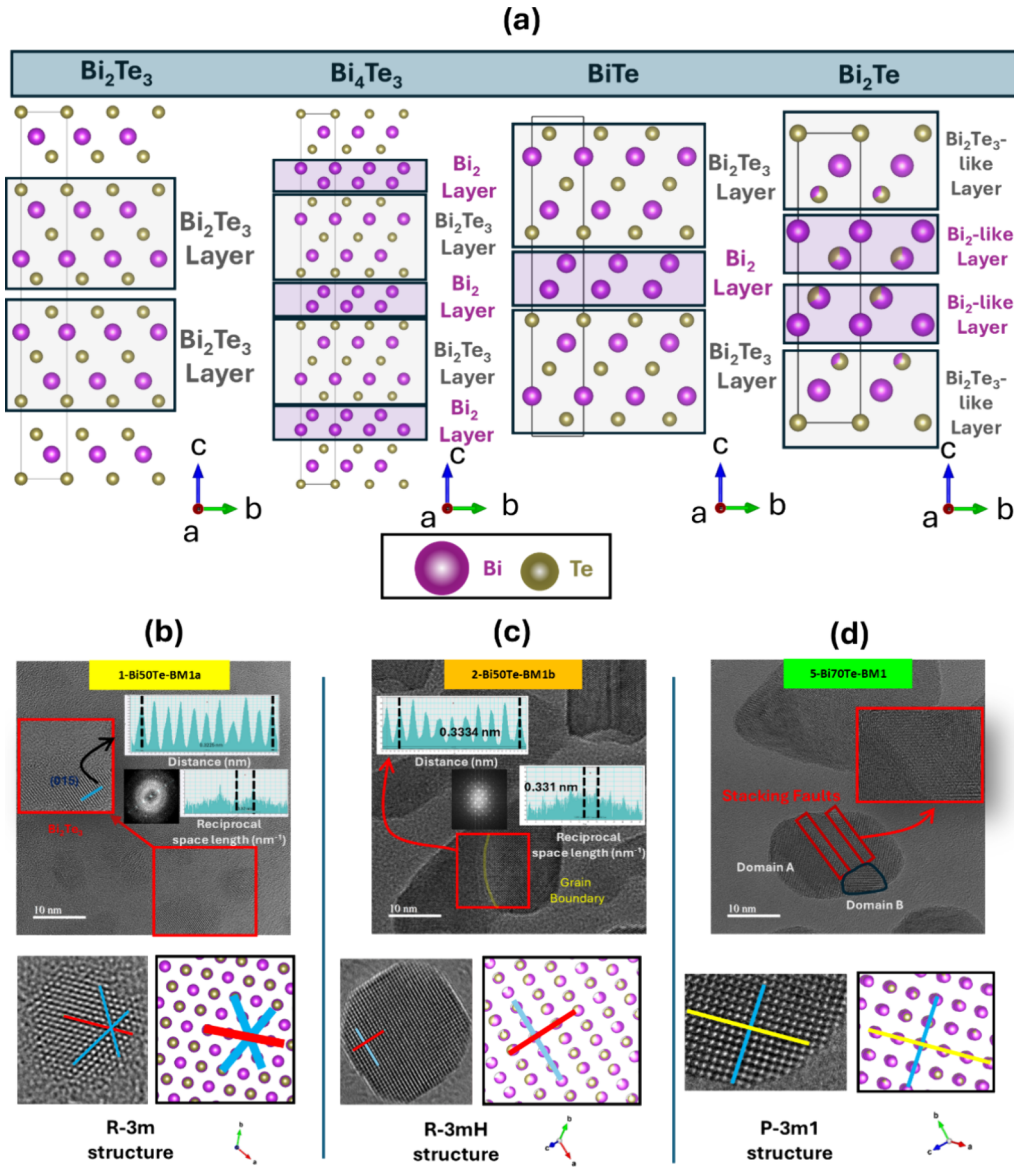

Figure 7. (a) Schematic representation of the layered structure of all the Bi−Te phases presented in the samples. Structural and microstructural TEM analysis of 1-Bi50Te-BM1a (b), 1-Bi50Te-BM1b (c), and 5-Bi70Te-BM1 (d).

https://doi.org/10.1021/acsaem.6c00972
ACS Appl. Energy Mater. 2026, 9, 6608−6621

nanocrystals shown in Figure 7b–d for some Bi–Te samples. In this case, the microscopies were directly compared with the structures simulated by VESTA.[51] Indeed, we observe that the Bi_2Te_3 phase present in the 1-Bi50Te-BM1a sample has a lower number of defects (stacking faults/grain boundaries). More details on the indexing of the interplanar distances are found in Table S5 of Supplementary Note 2.4

It is worth noting that sample 1-Bi50Te-BM1a exhibits very thin, irregular crystallites, in contrast to the more equiaxed morphologies observed in the other samples. This difference can be understood by considering the stacking sequences of the various Bi–Te phases, as illustrated in Figure 7a. In Bi_2Te_3, adjacent quintuple layers are separated by weak van der Waals interactions, with Te–Te interlayer distances of approximately 3.7 Å.[50] In contrast, phases such as BiTe contain additional Bi_2 layers, leading to shorter interlayer distances (e.g., Bi–Te ∼3.4 Å). This suggests that the bonding forces are stronger for the latter and thus less prone to exfoliation during milling and grid preparation for TEM analysis, resulting in a more equiaxed crystallite shape in BiTe. The same argument is made for the Bi_2Te phase present in the 5-Bi70Te-BM1 sample, where additional Bi_2–Bi_2-like layers are also present. Indeed, the separation between these layers is lower than the Bi_2Te_3–Bi_2Te_3 quintuple layers (∼3.55 Å). Additionally, the TEM micrographs show that the BiTe and Bi_2Te phases exhibit thicker, higher-contrast regions, suggesting denser stacking compared with Bi_2Te_3. Their higher layer thickness promotes more compact, quasi-spherical morphologies, while Bi_2Te_3, composed of thinner van der Waals-bonded layers, more readily forms plate-like or irregular shapes. To the best of our knowledge, no direct bond-energy comparison between these interfaces has been reported in the literature, so this remains a plausible structural interpretation of our TEM observations rather than a well-defined explanation.

Taken together, the results demonstrate that mechanical milling produces crystalline nanoparticles with polycrystalline character, organized into submicron agglomerates with predominantly lamellar morphology. This microstructure reproduces patterns previously reported in materials synthesized via bottom-up approaches,[50,52,53] supporting the validity and reproducibility of the present methodology. EDS spectra confirmed that the nominal Bi:Te ratio is preserved in all samples, despite significant oxygen contamination. The SEM images, EDS spectra, and the corresponding quantitative analysis are presented in Figure S14 of Supplementary Note 3. This analysis indicates that the grain-boundary scattering for both charge carriers and phonons will be significantly higher than highly dense bulk materials. To verify the assumptions, the TE characterization is given in the following.

3.4. TE Characterization

For TE characterization, the samples were consolidated into 16 mm diameter pellets by cold pressing (15 tons) followed by sintering (300 °C) under an Ar atmosphere to ensure stability during measurements. During pellet fabrication, sample 3-Bi50Te-BM2a underwent a phase transition and stabilized in the Tsumoite BiTe phase at room temperature. In addition, the Bi70Te sample showed partial decomposition into Bi. A detailed XRD analysis of these samples is provided in Supplementary Note 5. To assess the effect of densification, SPS samples were prepared using the as-milled 6-Bi70Te-BM2a powder.

The TE properties of the Bi_xTe_{100-x} samples are presented in Figure 8, while power factors, reversibility, and recyclability data are provided in Supplementary Note 6. It is important to note that several of the samples investigated are multiphase, as discussed in the structural characterization section. Therefore, the measured transport properties represent effective bulk responses of phase mixtures rather than intrinsic properties of a single crystalline phase. In particular, the coexistence of Bi–Te phases with oxide inclusions or secondary phases may introduce parallel conduction pathways and additional scattering mechanisms, which must be considered when interpreting the TE behavior.

In general, the electrical resistivity (ρ) increases with temperature (Figure 8a), consistent with degenerate semiconducting behavior. An exception is observed for sample 1-Bi50Te-BM1a, prepared from highly oxidized precursors, which exhibit significantly higher resistivity due to the presence of secondary oxide phases. Overall, resistivity increases with precursor oxidation level, following the trend 3-Bi50Te-BM2a < 2-Bi50Te-BM1b < 1-Bi50Te-BM1a, in agreement with EDS analysis (Supplementary Note 4). In particular, the formation of the ternary oxide $Bi_{0.82}Te_{0.18}O_{1.92}$ (*Fm*-3*m*, PDF #04-018-4267) in sample 1-Bi50Te-BM1a results in resistivity values several orders of magnitude higher than in the other samples. A similar trend is observed in the Seebeck coefficient (Figure 8b), where the highly oxidized sample exhibits larger S values. However, this increase does not translate into an improved power factor, which remains significantly lower (Figure S17, Supplementary Note 5). These results demonstrate that precursor oxidation deteriorates the electronic transport properties of $Bi_{50}Te_{50}$ samples, primarily due to the formation of insulating oxide phases. In this context, the observed transport behavior should be interpreted as arising from a composite system, where insulating oxide phases and conductive Bi–Te domains coexist, rather than from a homogeneous material.

To distinguish between the effects of oxidation and microstructural disorder, the role of structural defects was analyzed (Supplementary Note 5). For instance, sample 3-Bi50Te-BM2a exhibits a higher density of structural defects, including stacking faults, as evidenced by broader XRD peaks (Figure S15) and HR-TEM observations (Figure 7b). Despite this increased defect density, its electrical conductivity remains higher than that of the oxidized samples. This indicates that the reduced conductivity in oxidized materials is primarily governed by the formation of oxide phases rather than by defect- or grain-boundary-induced scattering. Consequently, the best electronic transport properties are obtained in samples synthesized from low-oxidation precursors, such as those prepared using the BM2 setup. In contrast, oxidation effects are less pronounced in $Bi_{70}Te_{30}$ samples, consistent with the lower oxidation tendency of Bi precursors (Table 1) and the corresponding transport data in Figure 8a,b.

The thermal conductivity (κ) further highlights the competing effects of oxidation and microstructure. As shown in Figure 8c, κ decreases with increasing precursor oxidation, with the lowest values obtained for sample 1-Bi50Te-BM1a containing the ternary oxide phase $Bi_{0.82}Te_{0.18}O_{1.92}$. This reduction is consistent with enhanced phonon scattering at defects, grain boundaries, and phase interfaces. As a result, a marked increase in the figure of merit ($zT = S^2/\rho\kappa T$) is observed (Figure 8d), making 1-Bi50Te-BM1a the best-performing material up to 250 °C. However, this apparent improvement arises from extrinsic effects associated with phase coexistence and reduced

https://doi.org/10.1021/acsaem.6c00972
ACS Appl. Energy Mater. 2026, 9, 6608–6621

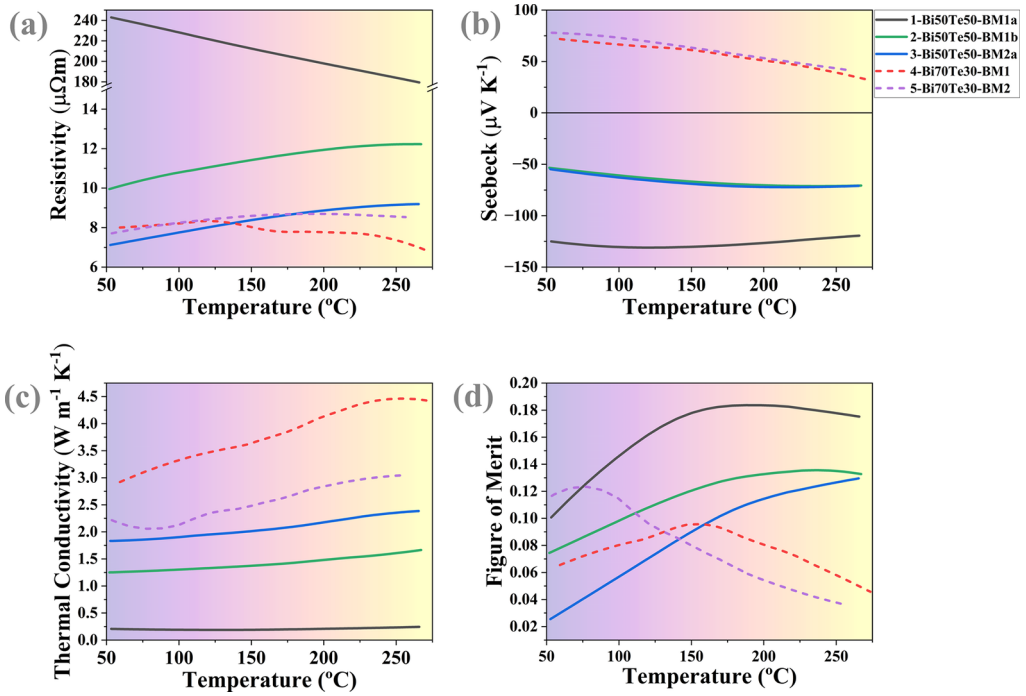

Figure 8. Thermoelectric characterization for the Bi−Te samples: (a) resistivity, (b) Seebeck coefficient, (c) thermal conductivity, and (d) figure of merit. The values of all the plots were smoothed for visualization purposes. Error estimates are 10% for all measurements.

density, rather than from intrinsically superior transport properties. Indeed, although BM2 samples are less crystalline than those produced via BM1 (SPEX-8000D), they exhibit higher κ, indicating that structural factors—particularly oxidation and the formation of secondary phases—play a dominant role in determining the TE performance. Therefore, while oxidation degrades the power factor of Bi–Te materials, the concurrent reduction in κ compensates for this effect in low-density samples, resulting in an overall increase in zT.

The transport properties discussed above correspond to samples prepared by cold pressing and sintering, which resulted in a comparable porosity level of approximately 20% for all materials due to identical pellet fabrication parameters (see Table S2, Supplementary Note 2). To further evaluate the role of extrinsic factors such as densification, the best-performing sample at room temperature (6-Bi70Te-BM2a) was consolidated by SPS, with the corresponding TE performance shown in Figure S22 (Supplementary Note 5). Owing to the layered van der Waals structure and strong electronic anisotropy of Bi–Te compounds, higher density and enhanced texture are expected to improve electronic transport. However, the electronic thermal conductivity (κ_{el}) becomes significant at elevated temperatures in the densified samples (Figure S20b), resulting in figure-of-merit values comparable to those of cold-pressed samples above 100 °C. Since ball-milled materials are particularly suitable for thin-film TE applications via ink formulation and spin-coating deposition,[54,55] where achieving high densification is often impractical, the performance of low-density samples provides a realistic assessment of their applicability in such devices.

3.5. Quality Factor

While the figure of merit (zT) is commonly used to evaluate TE performance, it does not necessarily reflect the intrinsic quality of a material. In practice, zT is highly sensitive to extrinsic factors such as porosity, microstructure, and carrier concentration, which depend on synthesis conditions and defect chemistry.[56] As a result, different sample preparation routes can lead to significant variations in zT by effectively shifting the chemical potential, without necessarily improving the intrinsic transport properties.

To better assess the intrinsic potential of the Bi–Te system, the TE quality factor (B) was evaluated. The B factor estimates the maximum achievable performance under optimal doping conditions and is therefore independent of extrinsic effects.[57] Within the single parabolic band (SPB) model, B depends on the weighted mobility (μ_w) and the lattice thermal conductivity (κ_L), capturing the intrinsic electronic and phonon transport properties of the material.[15] Further details on the calculation of B are provided in Supplementary Note 7.

In principle, μ_w should display similar temperature trends as the mobility measured by Hall-effect measurements (Figure 9a,b). These measurements reveal that the oxide-containing Bi_2Te_3-rich sample (1-Bi50Te-BM1a) exhibits a strongly reduced carrier mobility compared to the oxide-free BiTe sample (3-Bi50Te-BM2a). This reduction is not compensated by an increase in carrier concentration, indicating that oxide phases are intrinsically detrimental to charge transport. The suppression of mobility is attributed to enhanced carrier scattering and the disruption of conduction pathways by insulating oxide inclusions. A similar trend is observed in the weighted mobility (μ_w) (Figure 9c), confirming that the degradation of electronic transport originates from intrinsic limitations imposed by phase contamination. This effect is less pronounced in $Bi_{70}Te_{30}$ samples, consistent with the lower oxidation level of the Bi precursor. It should be noted that the presence of multiple crystalline phases introduces limitations in the interpretation of Hall-effect measurements, as the extracted carrier concentration and mobility represent averaged responses over all contributing phases rather than intrinsic properties of a single phase.

https://doi.org/10.1021/acsaem.6c00972
ACS Appl. Energy Mater. 2026, 9, 6608−6621

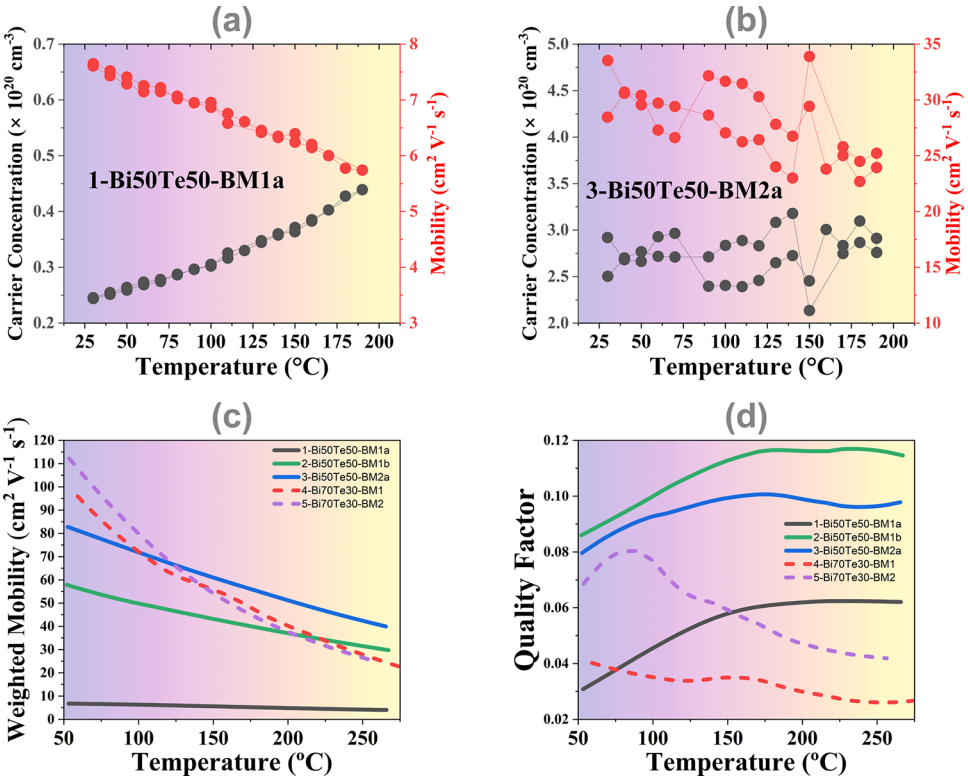

Figure 9. Carrier concentration and mobility for (a) 1-Bi50Te50-BM1a and (b) 3-Bi50Te50-BM2a samples. (c) Weighted mobility and (d) quality factor estimated with the thermoelectric data of Figure 8. Error estimates are 10% for all measurements.

When combining μ_w with the lattice thermal conductivity to evaluate the quality factor B (Figure 9d), a clear distinction emerges: oxide-free samples exhibit significantly higher B values—approximately twice those of the oxidized material. This demonstrates that, although the oxidized sample shows a higher zT due to its reduced thermal conductivity, its intrinsic transport properties are inferior. Consequently, under optimized doping and densification conditions, the oxide-free materials are expected to outperform the oxidized counterparts. This further supports the interpretation that the enhanced zT observed in multiphase samples is largely driven by extrinsic effects associated with phase coexistence, rather than by intrinsically superior transport properties.

Notably, densification has a limited impact on μ_w as reported in Figure S23 (Supplementary Note 6), indicating that intrinsic electronic transport remains largely unchanged. However, it increases B (see Figure S23c) by reducing porosity and modifying the balance between lattice and electronic thermal conductivity. Indeed, densification is necessary for achieving best performance in Bi–Te bulk device fabrication. However, thin film applications that rely on lower density materials,[55] this densification is not always possible, and the analysis provided in the current paper sheds some light on the TE properties of such low density samples.

4. CONCLUSIONS

In this study, rapid formation and stabilization of the structural and microstructural features of $Bi_{50}Te_{50}$ and $Bi_{70}Te_{30}$ were achieved within the first hour of ball milling. Both precursor oxidation and milling parameters were found to play a critical role in determining phase formation and the resulting TE properties. For the $Bi_{50}Te_{50}$ composition, three distinct crystalline phases were obtained depending on the oxidation level and processing conditions, all exhibiting n-type semiconducting behavior. In contrast, $Bi_{70}Te_{30}$ samples showed a weaker dependence on precursor oxidation, maintaining similar structural characteristics across different conditions and exhibiting p-type behavior. From a TE perspective, samples prepared under oxidizing conditions exhibited higher zT values due to a significant reduction in thermal conductivity, driven by the formation of oxide phases. However, this apparent improvement is accompanied by a substantial degradation of electronic transport, as evidenced by lower power factors and TE quality factors. These results demonstrate that, although oxidation can enhance zT through extrinsic effects, it deteriorates the intrinsic electronic performance of the material. Consequently, oxide-free Bi–Te compounds remain the most promising candidates for achieving optimal TE performance under fully optimized conditions. Finally, this work confirms mechanochemistry as a versatile and scalable route for synthesizing both n-type and p-type Bi–Te TE materials. Future efforts should focus on gaining deeper control over microstructural features—particularly stacking faults and layered disorder—to decouple thermal and electronic transport and further enhance performance.

■ ASSOCIATED CONTENT

Supporting Information

The Supporting Information is available free of charge at https://pubs.acs.org/doi/10.1021/acsaem.6c00972.

https://doi.org/10.1021/acsaem.6c00972
ACS Appl. Energy Mater. 2026, 9, 6608−6621

Additional experimental details, materials, and methods, including experimental data and analysis (DOCX)

AUTHOR INFORMATION

Corresponding Author

Carlos Eduardo Maduro de Campos – *Laboratório de Síntese e Caracterização de nanoMateriais - Departamento de Física, Universidade Federal de Santa Catarina, Florianópolis, Santa Catarina 88040-900, Brazil;* orcid.org/0000-0001-5475-5116; E-mail: carlos.campos@ufsc.br

Authors

Marcelo Augusto Malagutti – *Department of Civil, Environmental and Mechanical Engineering, University of Trento, via Mesiano 77, Trento 38123, Italy*; orcid.org/0000-0003-1053-4711

Rayner Enriquez Camps – *Laboratório de Síntese e Caracterização de nanoMateriais - Departamento de Física, Universidade Federal de Santa Catarina, Florianópolis, Santa Catarina 88040-900, Brazil*; orcid.org/0000-0003-4894-410X

Umberto Anselmi-Tamburini – *Department of Chemistry, University of Pavia, Pavia 27100, Italy*; orcid.org/0000-0002-8936-0170

Robert E. Dinnebier – *Max Planck Institute for Solid State Research, Heisenbergstrasse 1, Stuttgart 170569, Germany*; orcid.org/0000-0003-2778-2113

Claudia Weidenthaler – *Max-Planck-Institut für Kohlenforschung, Heterogeneous Catalysis, Kaiser-Wilhelm-Platz 1, Mülheim an der Ruhr 45470, Germany*; orcid.org/0000-0003-3006-1333

Paolo Scardi – *Department of Civil, Environmental and Mechanical Engineering, University of Trento, via Mesiano 77, Trento 38123, Italy*; orcid.org/0000-0003-1097-3917

Complete contact information is available at: https://pubs.acs.org/doi/10.1021/acsaem.6c00972

Funding

The Article Processing Charge for the publication of this research was funded by the Coordenacao de Aperfeicoamento de Pessoal de Nivel Superior (CAPES), Brazil (ROR identifier: 00x0ma614).

Notes

The authors declare no competing financial interest.

ACKNOWLEDGMENTS

Conselho Nacional de Desenvolvimento Científico e Tecnológico (CNPq grants 401246/2022-1 and 306590/2022-0), CAPES, and FAPESC. Federal university of Santa Catarina (UFSC) Multiuser facilities LDRX, LAMAF and, LCME. TEM, SEM-EDS measurements were performed at Stuttgart Center for Electron Microscopy (StEM) from MPI-FKF. We acknowledge DESY (Hamburg, Germany), a member of the Helmholtz Association HGF, for the provision of experimental facilities. Parts of this research were carried out at PETRA III, and we would like to thank Martin Etter for assistance in using P02.1. Beamtime was allocated for proposal I-20230188. We acknowledge MAX IV Laboratory for time on Beamline DanMAX. Research conducted at MAX IV is supported by the Swedish Research Council under contract 2018-07152, the Swedish Governmental Agency for Innovation Systems under contract 2018-04969, and Form as under contract 2019-02496. DanMAX is funded by the NUFI grant no. 4059-00009B. We are indebted to Maxwell W. Terban of Momentum Transfer for the measurements performed on a series of samples using beamline ID31 at the ESRF on summer of 2023, including high-resolution XRPD and total scattering measurements. The sixth author acknowledges the Italian Ministry of Education, Universities and Research (MUR) in the framework of the project DICAM-EXC (Departments of Excellence 2023-2027, grant L232/2016).

REFERENCES

(1) Mireles, V.; Stultz, J. W. Radioisotope Thermoelectric Generator Waste Heat System for the Cassini Propulsion Module. *J. Aerosp.* **1994**, *103*, 548–556.

(2) Narducci, D. Thermoelectric Harvesters and the Internet of Things: Technological and Economic Drivers. *J. Phys. Energy* **2019**, *1* (2), 024001.

(3) Mao, J.; Liu, Z.; Zhou, J.; Zhu, H.; Zhang, Q.; Chen, G.; Ren, Z. Advances in Thermoelectrics. *Adv. Phys.* **2018**, *67* (2), 69–147.

(4) Beretta, D.; Neophytou, N.; Hodges, J. M.; Kanatzidis, M. G.; Narducci, D.; Martin-Gonzalez, M.; Beekman, M.; Balke, B.; Cerretti, G.; Tremel, W.; Zevalkink, A.; Hofmann, A. I.; Müller, C.; Dörling, B.; Campoy-Quiles, M.; Caironi, M. Thermoelectrics: From History, a Window to the Future. *Mater. Sci. Eng., R: Rep.* **2018**, *2018* (138), 210–255.

(5) Artini, C.; Pennelli, G.; Graziosi, P.; Li, Z.; Neophytou, N.; Melis, C.; Colombo, L.; Isotta, E.; Lohani, K.; Scardi, P.; Castellero, A.; Baricco, M.; Palumbo, M.; Casassa, S.; Maschio, L.; Pani, M.; Latronico, G.; Mele, P.; Di Benedetto, F.; Contento, G.; De Riccardis, M. F.; Fucci, R.; Palazzo, B.; Rizzo, A.; Demontis, V.; Prete, D.; Isram, M.; Rossella, F.; Ferrario, A.; Miozzo, A.; Boldrini, S.; Dimaggio, E.; Franzini, M.; Galliano, S.; Barolo, C.; Mardi, S.; Reale, A.; Lorenzi, B.; Narducci, D.; Trifiletti, V.; Milita, S.; Bellucci, A.; Trucchi, D. M. Roadmap on Thermoelectricity. *Nanotechnology* **2023**, *34* (29), 292001.

(6) Brus, V. V.; Gluba, M.; Rappich, J.; Lang, F.; Maryanchuk, P. D.; Nickel, N. H. Fine Art of Thermoelectricity. *ACS Appl. Mater. Interfaces* **2018**, *10* (5), 4737–4742.

(7) Malagutti, M. A.; Lohani, K.; Caño Prades, I.; Navarro-Güell, A.; Bernard, T.; Chiappini, A.; Saucedo, E.; Ataollahi, N.; Scardi, P. $CuFeS_2/Cu_2S/FeS_2$ Composite to Increase the Performance of Thin-Film Thermoelectric Generators Based on Sustainable Materials. *ACS Appl. Electron. Mater.* **2025**, *7*, 21–32.

(8) Malagutti, M. A.; Lohani, K.; D'Incau, M.; Nautiyal, H.; Ataollahi, N.; Scardi, P. Optimizing $CuFeS_2$ Chalcopyrite Thin Film Synthesis: A Comprehensive Three-Step Approach Using Ball-Milling, Thermal Evaporation, and Sulfurization Applied for Thermoelectric Generation. *Appl. Sci.* **2023**, *13* (18), 10172.

(9) Bernard, T.; Malagutti, M. A.; Lohani, K.; D'Incau, M.; Ataollahi, N.; Scardi, P. Environmentally Friendly P-Type CTS-Based Thin-Film Thermoelectric Generator. *J. Mater. Sci.* **2024**, *59* (32), 15491–15503.

(10) Bernard, T.; Malagutti, M. A.; D'Incau, M.; Ataollahi, N.; Scardi, P. Sustainable Sulphides for π-Type Planar Thermoelectric Generators. *MRS Energy Sustainability* **2025**, 2.

(11) Goldsmid, H. J. *Introduction to Thermoelectricity*; Springer Series in Materials Science; Springer Berlin Heidelberg: Berlin, Heidelberg, **2016**; vol 121.

(12) Snyder, G. J.; Toberer, E. S. Complex TE Meterials. *Nat. Mater.* **2008**, *7*, 105–114.

(13) Goldsmid, H. J.; Douglas, R. W. The Use of Semiconductors in Thermoelectric Refrigeration. *Br. J. Appl. Phys.* **1954**, *5* (11), 386–390.
(14) Snyder, G. J.; Pereyra, A.; Gurunathan, R. Effective Mass from Seebeck Coefficient. *Adv. Funct. Mater.* **2022**, *32* (20), No. 2112772.
(15) Snyder, G. J.; Snyder, A. H.; Wood, M.; Gurunathan, R.; Snyder, B. H.; Niu, C. Weighted Mobility. *Adv. Mater.* **2020**, *32* (25), No. 2001537.
(16) Wei, J.; Yang, L.; Ma, Z.; Song, P.; Zhang, M.; Ma, J.; Yang, F.; Wang, X. Review of Current High-*zT* Thermoelectric Materials. *J. Mater. Sci.* **2020**, *55* (27), 12642–12704.
(17) Goldsmid, H. J. Bismuth Telluride and Its Alloys as Materials for Thermoelectric Generation. *Materials (Basel)* **2014**, *7* (4), 2577–2592.
(18) Witting, I. T.; Chasapis, T. C.; Ricci, F.; Peters, M.; Heinz, N. A.; Hautier, G.; Snyder, G. J. The Thermoelectric Properties of Bismuth Telluride. *Adv. Electron. Mater.* **2019**, *5* (6), No. 1800904.
(19) Ardila-Fierro, K. J.; Hernández, J. G. Sustainability Assessment of Mechanochemistry by Using the Twelve Principles of Green Chemistry. *ChemSusChem* **2021**, *14* (10), 2145–2162.
(20) Suryanarayana, C. Mechanical Alloying and Milling. *Prog. Mater. Sci.* **2001**, *46*, 1–189.
(21) Malagutti, M. A.; Paes, V. Z. C.; Geshev, J.; De Campos, C. E. M. Polymorphism of the Co–Te Nanophases in Mechanochemical Synthesis. *RSC Adv.* **2022**, *12*, 33488–33500.
(22) Malagutti, M. A.; De Fátima Ulbrich, K.; Paes, V. Z. C.; Geshev, J.; Maduro De Campos, C. E. Structural, Microstructural and Magnetic Characterization of the β-CoTe Nanophase Synthesized by a Novel Mechanochemical Method. *RSC Adv.* **2021**, *11* (9), 5027–5034.
(23) Isotta, E.; Fanciulli, C.; Pugno, N. M.; Scardi, P. Effect of the Order-Disorder Transition on the Seebeck Coefficient of Nanostructured Thermoelectric Cu_2ZnSnS_4. *Nanomaterials* **2019**, *9*, 762.
(24) Bos, J. W. G.; Zandbergen, H. W.; Lee, M.-H.; Ong, N. P.; Cava, R. J. Structures and Thermoelectric Properties of the Infinitely Adaptive Series $(Bi_2)_m(Bi_2Te_3)N$. *Phys. Rev. B* **2007**, *75* (19), No. 195203.
(25) Bos, J. W. G.; Faucheux, F.; Downie, R. A.; Marcinkova, A. Phase Stability, Structures and Properties of the $(Bi_2)_m(Bi_2Te_3)_n$ Natural Superlattices. *J. Solid State Chem.* **2012**, *193*, 13–18.
(26) Zhang, C. C.; Fan, X. A.; Hu, J.; Jiang, C. P.; Feng, B.; Xiang, Q. S.; Li, G. Q.; Li, Y. W. The Effect of Porosity and Milling Induced Defects on the Thermoelectric Properties of P-Type Bi_2Te_3-Based Bulks. *Adv. Eng. Mater.* **2016**, *18* (10), 1777–1784.
(27) Snyder, G. J.; Toberer, E. S. Complex Thermoelectric Materials. *Nat. Mater.* **2008**, *7*, 105–114.
(28) Liu, W.; Yan, X.; Chen, G.; Ren, Z. Recent Advances in Thermoelectric Nanocomposites. *Nano Energy* **2012**, *1* (1), 42–56.
(29) Martin-Gonzalez, M.; Lohani, K.; Neophytou, N. Phonon and Electron Transport Engineering for Enhanced Thermoelectric Performance and the Challenges of Device Integration. *Energy Mater.* **2025**, *5* (9), 500121.
(30) Zhao, X.; Zhu, X. H.; Zhang, R. Z. Evaluation of Energy Filtering Effect from First Principles Calculations. *Phys. Status Solidi: Appl. Mater. Sci.* **2016**, *213* (12), 3250–3253.
(31) Nolas, G. S.; Sharp, J.; Goldsmid, H. J. The Phonon—Glass Electron-Crystal Approach to Thermoelectric Materials Research. In *Thermoelectrics*; Springer: Berlin/Heidelberg, Germany, **2001**; pp 177–207.
(32) Puneet, P.; Podila, R.; Zhu, S.; Skove, M. J.; Tritt, T. M.; He, J.; Rao, A. M. Enhancement of Thermoelectric Performance of Ball-Milled Bismuth Due to Spark-Plasma-Sintering-Induced Interface Modifications. *Adv. Mater.* **2013**, *25* (7), 1033–1037.
(33) Coelho, A. A. TOPAS and TOPAS-Academic: An Optimization Program Integrating Computer Algebra and Crystallographic Objects Written in C++. *J. Appl. Crystallogr.* **2018**, *51* (1), 210–218.
(34) Rathmann, T.; Petersen, H.; Reichle, S.; Schmidt, W.; Amrute, A. P.; Etter, M.; Weidenthaler, C. In Situ Synchrotron X-Ray Diffraction Studies Monitoring Mechanochemical Reactions of Hard Materials: Challenges and Limitations. *Rev. Sci. Instrum.* **2021**, *92* (11), 114102.
(35) Kieffer, J.; Valls, V.; Blanc, N.; Hennig, C. New Tools for Calibrating Diffraction Setups. *J. Synchrotron Radiat.* **2020**, *27* (2), 558–566.
(36) Jensen, A. B.; Christensen, T. E. K.; Weninger, C.; Birkedal, H. Very Large-Scale Diffraction Investigations Enabled by a Matrix-Multiplication Facilitated Radial and Azimuthal Integration Algorithm: MatFRAIA. *J. Synchrotron Radiat.* **2022**, *29* (6), 1420–1428.
(37) Dippel, A.-C.; Liermann, H.-P.; Delitz, J. T.; Walter, P.; Schulte-Schrepping, H.; Seeck, O. H.; Franz, H. Beamline P02.1 at PETRA III for High-Resolution and High-Energy Powder Diffraction. *J. Synchrotron Radiat.* **2015**, *22* (3), 675–687.
(38) Schökel, A.; Etter, M.; Berghäuser, A.; Horst, A.; Lindackers, D.; Whittle, T. A.; Schmid, S.; Acosta, M.; Knapp, M.; Ehrenberg, H.; Hinterstein, M. Multi-Analyser Detector (MAD) for High-Resolution and High-Energy Powder X-Ray Diffraction. *J. Synchrotron Radiat.* **2021**, *28* (1), 146–157.
(39) Skinner, L. B.; Benmore, C. J.; Parise, J. B. Area Detector Corrections for High Quality Synchrotron X-Ray Structure Factor Measurements. *Nucl. Instruments Methods Phys. Res. Sect. A: Accel. Spectrometers, Detect. Assoc. Equip.* **2012**, *662* (1), 61–70.
(40) Schindelin, J.; Arganda-carreras, I.; Frise, E.; Kaynig, V.; Longair, M.; Pietzsch, T.; Preibisch, S.; Rueden, C.; Saalfeld, S.; Schmid, B.; Tinevez, J.; White, D. J.; Hartenstein, V.; Eliceiri, K.; Tomancak, P.; Cardona, A. Fiji: An Open-Source Platform for Biological-Image Analysis. *Nat. Methods* **2019**, *9*, 676–682.
(41) Klinger, M. More Features, More Tools, More CrysTBox. *J. Appl. Crystallogr.* **2017**, *50*, 1226–1234.
(42) Xu, H.; Song, Y.; Pan, W.; Chen, Q.; Wu, X.; Lu, P.; Gong, Q.; Wang, S. Vibrational Properties of Epitaxial Bi_4Te_3 Films as Studied by Raman Spectroscopy. *AIP Adv.* **2015**, *5*, 087103.
(43) Russo, V.; Bailini, A.; Zamboni, M.; Passoni, M.; Conti, C.; Casari, C. S.; Bassi, A. L.; Bottani, C. E. Raman Spectroscopy of Bi-Te Thin Films. *J. Raman Spectrosc.* **2008**, *39*, 205–210.
(44) Kuznetsov, P. I.; Yapaskurt, V. O.; Shchamkhalova, B. S.; Shcherbakov, V. D.; Yakushcheva, G. G.; Luzanov, V. A.; Jitov, V. A. Growth of Bi_2Te_3Fi Lms and Other Phases of Bi-Te System by MOVPE. *J. Cryst. Growth* **2016**, *455*, 122–128.
(45) Galva, M.; Torres-costa, V.; Climent-font, A.; Concepcio, O.; Escobosa, A.; Melo, O. De; Bahena, D.; Manso, M. Controlling the Epitaxial Growth of Bi_2Te_3, BiTe, and Bi_4Te_3 Pure Phases by Physical Vapor Transport. *Inorg. Chem.* **2018**, *57*, 10090–10099.
(46) Caballero-Calero, O.; Manzano, C. V.; Cantarero, A.; Martín-González, M. Geometry-Driven Plasmonic Heating in Bi_2Te_3 Nanostructures Intrinsic Surface Plasmons Enable Enhanced Thermoelectric Voltage. *Chem. Eng. J.* **2025**, *523*, No. 168220.
(47) Qi, X.; Ma, W.; Zhang, X.; Zhang, C. Applied Surface Science Raman Characterization and Transport Properties of Morphology-Dependent Two-Dimensional Bi_2Te_3 Nano Films. *Appl. Surf. Sci.* **2018**, *457*, 41–48.
(48) Shahil, K. M. F.; Hossain, M. Z.; Goyal, V.; Balandin, A. A. Micro-Raman Spectroscopy of Mechanically Exfoliated Few- Quintuple Layers of Bi_2Te_3, Bi_2Se_3, and Sb_2Te_3 Materials?. *J. Appl. Phys.* **2014**, *111*, 054305.
(49) Caha, O.; Dubroka, A.; Holy, V.; Steiner, H.; Rader, O.; Stanislavchuk, T. N.; Sirenko, A. A.; Bauer, G.; Springholz, G. Growth, Structure, and Electronic Properties of Epitaxial Bismuth Telluride Topological Insulator Films on $BaF_2(111)$ Substrates. *Cryst. Growth Des.* **2013**, *2*, 3365–3373.
(50) Akshay, V. R.; Suneesh, M. V.; Vasundhara, M. Tailoring Thermoelectric Properties through Structure and Morphology in Chemically Synthesized N-Type Bismuth Telluride Nanostructures. *Inorg. Chem.* **2017**, *56* (11), 6264–6274.
(51) Momma, K.; Izumi, F. VESTA: A Three-Dimensional Visualization System for Electronic and Structural Analysis. *J. Appl. Crystallogr.* **2008**, *41* (3), 653–658.
(52) Son, J. S.; Choi, M. K.; Han, M.-K.; Park, K.; Kim, J.-Y.; Lim, S. J.; Oh, M.; Kuk, Y.; Park, C.; Kim, S.-J.; Hyeon, T. N-Type Nanostructured Thermoelectric Materials Prepared from Chemically Synthesized Ultrathin Bi_2Te_3 Nanoplates. *Nano Lett.* **2012**, *12* (2), 640–647.
(53) Soni, A.; Yanyuan, Z.; Ligen, Y.; Aik, M. K. K.; Dresselhaus, M. S.; Xiong, Q. Enhanced Thermoelectric Properties of Solution Grown

https://doi.org/10.1021/acsaem.6c00972
ACS Appl. Energy Mater. 2026, 9, 6608–6621

$Bi_2Te_{3-x}Se_x$ Nanoplatelet Composites. *Nano Lett.* **2012**, *12* (3), 1203–1209.
(54) Isotta, E.; Syafiq, U.; Ataollahi, N.; Chiappini, A.; Malerba, C.; Luong, S.; Trifiletti, V.; Fenwick, O.; Pugno, N.; Scardi, P. Thermoelectric Properties of CZTS Thin Films: Effect of Cu-Zn Disorder. *Phys. Chem. Chem. Phys.* **2021**, *23*, 13148–13158.
(55) Syafiq, U.; Isotta, E.; Ataollahi, N.; Lohani, K.; Luong, S.; Trifiletti, V.; Fenwick, O.; Scardi, P. Facile and Low-Cost Fabrication of Cu/Zn/Sn-Based Ternary and Quaternary Chalcogenides Thermoelectric Generators. *ACS Appl. Energy Mater.* **2022**, *5* (5), 5909–5918.
(56) Pei, Y.; Shi, X.; LaLonde, A.; Wang, H.; Chen, L.; Snyder, G. J. Convergence of Electronic Bands for High Performance Bulk Thermoelectrics. *Nature* **2011**, *473* (7345), 66–69.
(57) Zhang, X.; Bu, Z.; Shi, X.; Chen, Z.; Lin, S.; Shan, B.; Wood, M.; Snyder, A. H.; Chen, L.; Snyder, G. J.; Pei, Y. Electronic Quality Factor for Thermoelectrics. *Sci. Adv.* **2020**, *6* (46), No. eabc0726.

https://doi.org/10.1021/acsaem.6c00972
ACS Appl. Energy Mater. 2026, 9, 6608–6621